Coherent Raman spectroscopy on hydrogen with in-situ generation, in-situ use, and in-situ referencing of the ultrabroadband excitation

Mazza, Francesco; Stutvoet, Aert; Castellanos, Leonardo; Kliukin, Dmitrii; Bohlin, Alexis

DOI
10.1364/OE.465817

Publication date
2022

Document Version
Final published version

Published in
Optics Express

Research Article | Vol. 30, No. 20 / 26 Sep 2022 / Optics Express 35232
Optics EXPRESS

Coherent Raman spectroscopy on hydrogen with *in-situ* generation, *in-situ* use, and *in-situ* referencing of the ultrabroadband excitation

Francesco Mazza,[1] Aert Stutvoet,[1] Leonardo Castellanos,[1] Dmitrii Kliukin,[1,2] and Alexis Bohlin[1,3,*]

[1] *Faculty of Aerospace Engineering, Delft University of Technology, Kluyverweg 1, 2629 HS Delft, The Netherlands*
[2] *LaserLaB, Department of Physics and Astronomy, Vrije Universiteit Amsterdam, De Boelelaan 1081, 1081 HV Amsterdam, The Netherlands*
[3] *Space Propulsion Laboratory, Department of Computer Science, Electrical and Space Engineering, Luleå University of Technology, 98128 Kiruna, Sweden*
[*] *alexis.bohlin@ltu.se*

Abstract: Time-resolved spectroscopy can provide valuable insights in hydrogen chemistry, with applications ranging from fundamental physics to the use of hydrogen as a commercial fuel. This work represents the first-ever demonstration of *in-situ* femtosecond laser-induced filamentation to generate a compressed supercontinuum behind a thick optical window, and its *in-situ* use to perform femtosecond/picosecond coherent Raman spectroscopy (CRS) on molecular hydrogen (H_2). The ultrabroadband coherent excitation of Raman active molecules in measurement scenarios within an enclosed space has been hindered thus far by the window material imparting temporal stretch to the pulse. We overcome this challenge and present the simultaneous single-shot detection of the rotational H_2 and the non-resonant CRS spectra in a laminar H_2/air diffusion flame. Implementing an *in-situ* referencing protocol, the non-resonant spectrum measures the spectral phase of the supercontinuum pulse and maps the efficiency of the ultrabroadband coherent excitation achieved behind the window. This approach provides a straightforward path for the implementation of ultrabroadband H_2 CRS in enclosed environment such as next-generation hydrogen combustors and reforming reactors.

1. Introduction

Molecular hydrogen (H_2) is the object of an ever-increasing scientific interest, in view of its prospect use as the main energy carrier in the current energy transition [1], and a significant research effort is being spent on the development of technologies enabling H_2-based carbon-neutral combustion. The experimental investigation of H_2 chemistry [2,3], which plays a significant role in its storage and utilization, requires the availability of time-resolved spectroscopic techniques, providing information on the molecular dynamics on picosecond (ps) and femtosecond (fs) timescales [4]. The current state-of-the-art technique for gas-phase molecular spectroscopy is coherent Raman scattering (CRS) spectroscopy [5], which has found vast application to high fidelity *in-situ* measurements of the temperature field and chemical flow composition in combustion environments [6,7], and in non-equilibrium thermodynamic systems [8,9]. Since the first observation of rotational coherent Raman scattering in gas-phase media [10], CRS has been successfully demonstrated in gaseous H_2, both as a test-bench for fundamental physics (e.g. dynamic Stark effect [11]) and for enabling the development of novel photonic technologies [12]. Despite the research effort spent over the years, the application of CRS techniques to perform direct broadband multiplex spectroscopy on H_2 still presents a significant challenge due to sparse ro-vibrational energy manifold of the H_2 molecule [13]. Vibrational H_2 CRS

#465817 https://doi.org/10.1364/OE.465817
Journal © 2022 Received 1 Jun 2022; revised 25 Aug 2022; accepted 25 Aug 2022; published 13 Sep 2022

Optics EXPRESS

spectroscopy has been applied in combustion environments [14], as well as in plasmas [15], by employing broadband nanosecond dye lasers. Further development of H_2 CRS has been more recently promoted by the availability of ultrafast regenerative laser amplifiers, producing pulses a few tens of fs long, which have sprung the development of time-resolved spectroscopic techniques to investigate chemical reactions in real time [16]. Lang *et al.* were the first to employ fs pulses to perform coherent anti-Stokes Raman spectroscopy (CARS) on H_2, resolving the temporal dynamics of its ro-vibrational wave packet with sub-ps resolution [17]. Tran *et al.* used fs-CRS to study the H_2-N_2 collisional system and the speed-memory effects due to the high motility of the H_2 molecules [18]. Magnitskiĭ and Tunkin investigated the Dicke narrowing of the H_2 Q-branch, using ps-CRS to measure its coherence lifetime with high temporal and spectral resolution [19]; similar ps-CRS measurements of the H_2 Q-branch coherence lifetime were performed by Kulatilaka *et al.* [20]. The idea of combining broadband fs pulses to generate maximal quantum coherence of the Raman-active molecules [21] and relatively-narrowband ps pulses to perform simultaneously temporally- and spectrally-resolved measurements [22] has led to the development of hybrid fs/ps CRS [23]. The introduction of ultrabroadband fs laser sources greatly enhanced the spectral interrogation window of fs/ps CRS [24], allowing for the detection of virtually all the rotationally Raman-active species in the probed volume and for the investigation of their chemistry. Bohlin and Kliewer [25] demonstrated the use of a ~7 fs compressed supercontinuum, generated in an argon-filled hollow-core fiber, to simultaneously excite both the pure-rotational H_2 S-branch and the vibrational H_2 Q-branch transitions, in the range 0-4200 cm^{-1}. Despite the huge versatility of ultrabroadband fs/ps CRS, its application to perform measurements behind thick optical windows is limited by the significant chirp that these impart to broadband [26] and ultrabroadband fs pulses.

In the present work, we employ fs laser-induced filamentation [27] to generate a compressed supercontinuum pulse *in-situ*, where it is employed as a single pump/Stokes excitation pulse [28] to drive the pure-rotational Raman coherence up to ~1500 cm^{-1}. This approach is combined

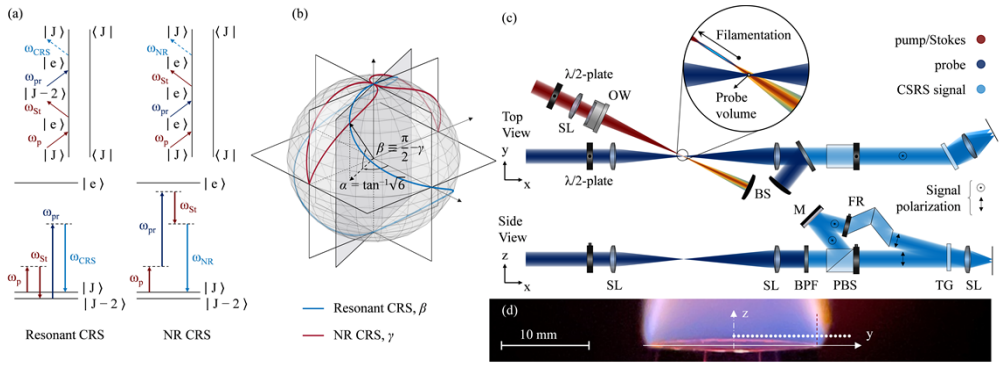

Fig. 1. (a) Energy and Feynman diagrams of a resonant (left) and a non-resonant (right) CRS pathways. (b) Polarization angles of the resonant (blue line) and non-resonant (red line) CRS signals, β and γ, represented as the elevation angle on the unit sphere as a function of the relative polarization angle (azimuthal angle) of the pump/Stokes and probe fields, α. (c) Schematic of the polarization-sensitive coherent imaging spectrometer. OW, optical window; SL, spherical lenses; M, mirror; BPF, band-pass filter; PBS, polarization beam splitter; FR, Fresnel rhomb; BS, beam stop. Inset: probe volume. The probe crosses the ultrabroadband pump/Stokes beam ~2mm after the end of the filament. The increment of input energy results in the elongation of the filament towards the focusing optics (arrow direction) (d) Measurements points across the H_2/air flame front, the dashed red line identifies the location of the burner rim at y = 9.5 mm.

Optics EXPRESS

with the simultaneous shot-to-shot measurement of the non-resonant (NR) CRS signal, due to the instantaneous electronic optical response of the medium (Fig. 1(a)), to map the spectral efficiency of the coherent excitation, which can significantly impact the accuracy and precision of the H_2 spectroscopy [29]. We use a polarization approach to simultaneously generate and detect the resonant and NR CRS signals with orthogonal polarization [30], as shown in Fig. 1(b). This *in-situ* spectral referencing allows us to monitor the spectrochronographic properties of the compressed supercontinuum and the bandwidth of the coherent Raman excitation. We demonstrate the application of fs/ps H_2 CRS with *in-situ* generation, use and referencing of the ultrabroadband coherent excitation to perform thermometric measurements in a laminar H_2/air diffusion flame as shown in Fig. 1(d), and to experimentally demonstrate preferential diffusion of H_2 [31].

2. Theory and methods

2.1. Analytical framework

The excitation efficiency of the H_2 Raman active modes depends on the spectrochronographic characteristics of the broadband pump/Stokes pulse, and is effectively controlled by its spectral phase [32,33], as shown in the application of coherent control theory to CRS [34,35]. We measure the excitation bandwidth provided by the combined pump/Stokes pulse using the intensity spectrum of the NR CRS signal. The NR CRS signal is here modelled in the time domain under the assumptions of instantaneous dephasing of the electronic coherence induced by the non-resonant two-photon excitation pathways in Fig. 1(a) and temporal overlap of the probe field E_3 with the pump/Stokes field E_{12} [24]:

$$P_{\mathrm{NR}}^{(3)}(t) = \left(\frac{i}{\hbar}\right)^3 \chi_{\mathrm{NR}}^{(3)} \cdot E_3(t) \cdot E_{12}^*(t) \cdot E_{12}(t) \tag{1}$$

The pump/Stokes pulse is assumed to have a Gaussian envelope in the time domain with duration Δt_{12} (FWHM):

$$E_{12}(t) \propto \exp[-2\ln 2(t - t_{12})^2/\Delta t_{12}^2] \cdot \exp(i\omega_{12}t) + c.c. \tag{2}$$

with t_{12} being the arrival time of the combined pump/Stokes pulse, and ω_{12} the carrier (angular) frequency of the pulse ($\omega_{12} = 2.34$ rad/fs for 806.7 nm). The spectrum of the NR CRS field, resulting from the pump/Stokes photon-pairs found across the instantaneous bandwidth of the pulse, is then computed via the Fourier transform of Eq. (1), and is thus proportional to the spectral autocorrelation of the pump/Stokes laser field [36]:

$$P_{\mathrm{NR}}^{(3)}(\omega) \propto \chi_{\mathrm{NR}}^{(3)} E_3(\omega) * [E_{12}(\omega) \star E_{12}(\omega)] \tag{3}$$

$$I_{\mathrm{NR}}(\omega) \propto |\chi_{\mathrm{NR}}^{(3)} E_3(\omega) * [E_{12}(\omega) \star E_{12}(\omega)]|^2 \tag{4}$$

where $\star$ and $*$ represent the cross-correlation and convolution operators, respectively. Hence, the intensity spectrum in Eq. (4) is used to measure the spectral autocorrelation of the fs pump/Stokes pulse and deduce information on its spectral phase. Equation (2) and Eq. (4) are employed to generate a library of synthetic NR CRS spectra for varying pulse duration, and fit the experimental NR CRS spectra acquired in a non-resonant gas (e.g. methane or argon) flow. The spectral phase of the pump/Stokes pulse is introduced in the model through the Taylor expansion:

$$\varphi(\omega) = \sum_n L \cdot k_{(n)}(\omega_{12}) \cdot \frac{(\omega - \omega_{12})^n}{n!} \tag{5}$$

with L being the thickness of the optical window, and $k_{(n)}$ the n^{th}-order derivative of the wave vector $k(\omega)$ in the dispersive medium ($k_{(2)}$ thus representing the group velocity dispersion of the

Optics EXPRESS

fs pulse). The chirped pump/Stokes pulse is thus represented in the frequency domain as:

$$E_{12}(\omega) \propto \exp\left[-2\ln 2(\omega-\omega_{12})^2/\Delta\omega_{12}^2\right] \cdot \exp\left[-i\sum_n \varphi_{(n)} \cdot \frac{(\omega-\omega_{12})^n}{n!}\right] \tag{6}$$

Substituting Eq. (6) into Eq. (3), the spectral autocorrelation of the pump/Stokes pulse is computed according to the integral:

$$(E_{12} \star E_{12})(\Omega) = \int_{-\infty}^{\infty} d\omega E_{12}^*(\omega) E_{12}(\omega+\Omega) \propto \exp\left[-\left(\frac{\ln 2}{\Delta\omega_{12}^2} + i\frac{\varphi_2}{2}\right)\Omega^2\right] \cdot \int_{-\infty}^{\infty} d\omega \exp\left\{\frac{4\ln 2}{\Delta\omega_{12}^2}\left[\Omega + \frac{(\omega-\omega_{12})}{2}\right]^2 - i\varphi_2\Omega\frac{(\omega-\omega_{12})}{2}\right\} \tag{7}$$

where only the quadratic phase term (φ_2) has been included. Note that including the third-order dispersion (TOD, φ_3) would only contribute to the real part of the argument of the exponential integrand, as the imaginary part factors out in the product with the complex-conjugated field: this is true for all the odd terms in the spectral phase expansion of Eq. (5). A closed-form solution to the integral in Eq. (7) is given in the form:

$$(E_{12} \star E_{12})(\Omega) \propto \sqrt{\pi(4\log 2 + i\varphi_2\Delta\omega_{12}^2)} \exp\left[\left(-\frac{4\ln 2}{\Delta\omega_{12}^2} + i\varphi_2\right)\Omega^2\right] \tag{8}$$

which represents a Gaussian envelope modulated by non-linear harmonic oscillations, having the form of the derivative of Fresnel sine integral function, with local frequency proportional to the quadratic phase term. Equation (4) and Eq. (8) are employed to generate a library of synthetic NR CRS spectra for varying pulse duration, and fit the experimental NR CRS spectra, as shown in Fig. 2.

2.2. Experimental setup

The laser system employed for ultrabroadband fs/ps CRS spectroscopy is detailed in Ref. [37]. A single ultrafast regenerative amplifier system (Astrella, Coherent) combined with a second-harmonic bandwidth compressor unit (Light Conversion), provides the combined pump/Stokes (35 fs, 1650 μJ/pulse at 806.7 nm) and the probe (12.6 ps, 117 μJ/pulse at 403.4 nm) fields which are auto-synchronized at 1 kHz repetition rate and focused to the measurement location using spherical lenses (f: 500 and 300 mm, respectively). We demonstrate its applicability to measurements behind thick optical windows by transmitting the fs beam through a ~22 mm thick BK7 glass window. This glass has larger group velocity dispersion at 800 nm (~45 fs^2/mm) than other optical window materials (e.g. fused silica ~36 fs^2/mm), which demonstrates the application of this methodology to the more extreme conditions. The window is placed ~200 mm after the focusing lens to prevent white light generation inside the glass. The energy of the fs beam after the transmission thought the optical window is ~1500 μJ/pulse. We control the temporal chirp of the fs pulse prior the *in-situ* filamentation using an external pulse-compressor. Thin-film polarizers ensure the linear polarization of the pump/Stokes and the probe beams, and half-wave plates control their polarization angles. Ensuring the linearity of the polarization of the fs beam before it undergoes filamentation is critical to control the polarization state of the compressed supercontinuum, since electronic Kerr nonlinearity, electron plasma, and molecular alignment in the filament result in the rotation of the polarization ellipse [38]. Linearly polarized pulses maintain their polarization state in fs laser-induced filamentation and in the post-filamentation propagation [39]. Adopting a two-beam nearly phase-matched configuration

Optics EXPRESS

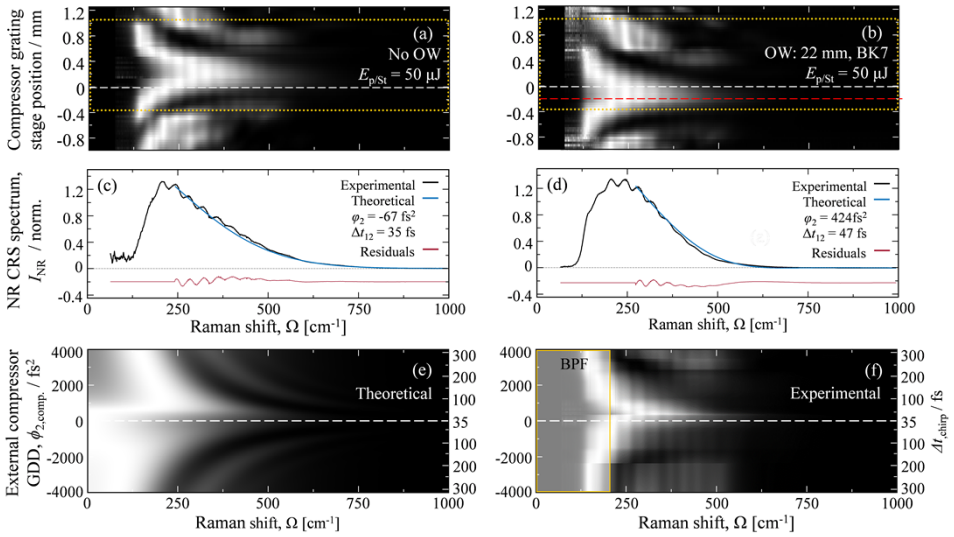

Fig. 2. (a) 1000-shot-averaged NR CRS spectra recorded, by varying the position of the compressor grating, in a flow of CH_4 without the optical window (No OW). The white dashed line identifies the condition of a near transform-limited (TL) pulse. (b) Corresponding NR CRS spectra after the introduction of a BK7 optical window (OW) in the pump/Stokes beam path. The red dashed line identifies the condition of a TL pulse obtained after transmission through the window. The dotted boxes represent the region of interest (ROI) analyzed in the present work. (c) NR CRS spectrum for a near TL pump/Stokes pulse as compared to the time-domain NR CRS model (No OW). (d) NR CRS spectrum for TL pump/Stokes pulse transmitted through the optical window (OW). (e) NR CRS signal for varying linear chirp in the input fs pump/Stokes pulse, as predicted by the time-domain model. For values of the pulse GDD larger than ~1000 fs^2 the spectral autocorrelation of the pulse results in the formation of sidebands in the CRS spectrum and in the narrowing of the excitation window. (f) Experimental autocorrelation of the fs pulse as measured by the NR CRS signal of room temperature CH_4 in the ROI. The opaque box represents the spectral region affected by the edge of the band pass filter (BPF).

[28], the pump/Stokes beam is crossed by the probe beam ~2 mm after the end of the filament to avoid ionization inside the probe volume. The ending point of the filamentation generated both across the flame and in non-resonant gases (i.e. argon and methane) is always fixed regardless of the input pulse energy and the local thermodynamic properties of the gas [37]. The resulting dimensions of the probe volume are thus estimated geometrically to be 20 µm (width, FWHM) x 2.5 mm (length, FWHM) x 20 µm (height, FWHM). The coherent imaging spectrometer developed for the simultaneous acquisition of the resonant and NR CRS signals in Ref. [30] is here adapted for the *in-situ* referencing of the ultrabroadband excitation generated in the flame. A Fresnel Rhomb rotates the polarization of the NR signal to maximize the efficiency of a high-resolution transmission diffraction grating (>90% diffraction efficiency for S-polarization, Ibsen Photonics). The signals are imaged onto the sCMOS detector (Zyla, Andor) through a fast-focusing lens (f: 100 mm), resulting in a detection bandwidth of 1900 cm^{-1}, with a dispersion of 0.93 cm^{-1}/pixel. The resolution of the H_2 CRS spectra is limited by the linewidth of the ps probe pulse which is measured to be ~2.7 cm^{-1}, and by the instrumental broadening of the spectrometer, which is fitted to a Voigt profile with a ~0.1 cm^{-1} FWHM Lorentzian and a ~1.7 cm^{-1} FWHM Gaussian contribution. For high-resolution spectroscopy in the pure-rotational region (~50-600 cm^{-1}) the spectrometer is adapted by changing the imaging lens to a slower

Optics EXPRESS

focus (f: 400 mm), resulting in a dispersion of ~0.27 cm^{-1}. H_2 CRS measurements were performed across the flame front of a laminar H_2/air diffusion flame, provided on a Bunsen burner: the probe volume was moved from the center of the burner towards its rim, in steps of 0.5 mm as shown in Fig. 1(d). A steel mesh was placed ~15 mm above the burner to stabilize the flame and the measurements were performed ~0.5 mm (H_2 CRS thermometry) and ~1 mm (preferential diffusion) above its nozzle. The H_2 flow was diluted in a 50% mixture with nitrogen (N_2) to perform conventional N_2 CRS thermometry for validation purposes. The *ex-situ* spectral referencing protocol is performed by measuring the NR CRS signal from the compressed supercontinuum generated in a flow of room temperature argon (which has no rotational degree of freedom).

3. Results

3.1. Autocorrelation measurements of the fs pump/Stokes pulse

The effect of temporal chirp in the pump/Stokes pulse on the spectral excitation efficiency is illustrated in Fig. 2. 1000-shot-averaged NR CRS spectra were recorded as a function of the pulse dispersion, controlled by the external compressor unit in Fig. 2 (a) and introduced by the optical window in Fig. 2 (b), in a non-resonant gas flow (methane, CH_4). The input pump/Stokes pulse energy was 50 μJ, i.e. lower than the filamentation onset. The amount of chirp in the input pulse is controlled by varying the angle of the diffraction grating in the external compressor unit (details in Supplement 1). A strong periodic modulation of the NR CRS spectra in Fig. 2(a) results from the introduction of quadratic phase to the pump/Stokes pulse, in accordance with the theoretical result of Eq. (8). The pulse transmission through the thick optical material only introduces linear chirp, as proven by the translation of the spectrochronogram from Fig. 2(a) to Fig. 2(b). The dependence of the NR CRS spectrum on the spectral phase of the pump/Stokes pulse can be exploited to measure its spectrochronographic properties: we do this by fitting the experimental spectra to our time-domain NR CRS model. We quantify the quadratic phase introduced by the external compressor, resulting in a stretching of the 35 fs near transform-limited (TL) pump/Stokes pulse in Fig. 2(c) to ~150 fs by either negative or positive dispersion. The same input chirp is combined with transmission through the window in Fig. 2(d), allowing for a direct evaluation of the positive group delay dispersion (GDD) arising due to the optical material: this is measured to be 424 fs^2, resulting in a stretching of the pulse duration to 47 fs. When the combined GDD is larger (in magnitude) than ~1000 fs^2, the autocorrelation of the pump/Stokes pulse results in the shift of the local maximum of the spectral excitation in the range ~300-1000 cm^{-1}, evident in the raw data of Fig. 2(a-b). For large pulse GDD, the NR CRS spectrum departs from the usual monotonic trend with the Raman shift, presenting multiple local maxima at locations which depend on the GDD itself. This behavior is similar to what has been shown by applying spectral focusing [40] and pulse shaping [41] techniques, but is here realized without any intra-pulse delay as our CRS system employs a single combined pump/Stokes pulse. Figure 2(e-f) shows the comparison of the experimental and the theoretical spectral autocorrelation of the fs pump/Stokes pulse as measured by the NR CRS signal. The time-domain CRS model illustrated by Fig. 2(e) predicts the parallel formation of spectral sidebands: this prediction is experimentally verified in Fig. 2(f). This behavior is analogous to the spectral focusing technique first demonstrated by T. Hellerer *et al.* [42] for CARS microscopy: introducing the same amount of GDD in their broadband fs pump and Stokes pulses, they demonstrated the coherent excitation of a narrow spectral region with spectral selectivity enabled by the tuning of the intrapulse delay. The experimental NR CRS spectra in Fig. 2(f) thus map the effect of the linear chirp in the input fs pulse, which results in the narrowing of the spectral excitation, and in its shift to values of the Raman shift $|\Omega| > 0$, even with a null intrapulse delay for our combined pump/Stokes pulse.

Optics EXPRESS

3.2. Generation of ultrabroadband coherent excitation behind the optical window

The use of ultrabroadband CRS techniques at measurement scenarios with an enclosed space (e.g. high-pressure combustors, optical cells, etc.) requires the experimentalist to maintain control of the spectral phase while the compressed supercontinuum pulse is transported through the optical windows, which is impractical, perhaps even impossible. In the present work we demonstrate that fs laser-induced filamentation [43,44] can be used to generate a compressed supercontinuum pulse *in-situ* behind an optical window, thus maximizing the rotational Raman coherence in gaseous H_2. The time-domain NR CSR model is extended to the ultrabroadband NR signal generated by the compressed supercontinuum acting as the pump/Stokes pulse. We let the duration of the fs pulse vary and used it as an additional fitting parameter, thus accounting for the increment of the pulse bandwidth due to its self-phase modulation in the filamentation process. The temporal compression of the resulting spectrally-broadened pulse, due to its non-linear propagation in the plasma medium, is again modelled by the GDD of the medium. The most stringent assumption introduced here is that of a symmetric broadening of the pulse spectrum, preserving its original Gaussian shape. The validity of this assumption could be limited when the pulse is compressed in air under tight focusing conditions: if the contribution of the non-linear refractive index of the dense plasma medium to self-phase modulation is greater than the one due to Kerr effect, an asymmetric broadening of the pulse spectrum would result to higher frequencies. Within the scope of the present work we nonetheless find the assumption reasonable, given the limited energy of the input fs pulse and the much-reduced density of the plasma generated in the hot environment of the flame. The pulse compression achieved via fs laser-induced filamentation can also be experimentally investigated as a function of the linear chirp in the input fs pulse, as shown in Fig. 3. The generation of the compressed supercontinuum in the filament depends on the complex interplay between multiple non-linear optical processes, whose relative magnitude is determined by the non-linear susceptibility of the gaseous medium where the filament is generated. While for non-resonant molecules (e.g. argon) the third-order non-linear susceptibility is entirely electronic in nature, the generation of rotational nuclear wave packets in Raman-active molecules (e.g. N_2 and O_2) can play a role in the pulse compression through self-phase modulation and non-linear light propagation. This explain the different output of the filamentation process, in terms of pulse compression and corresponding ultra-broad excitation bandwidth, in CH_4 and in air.

Figure 3(b) shows the ultrabroadband NR CRS spectra acquired in a room-temperature flow of CH_4, as a function of the linear chirp in the input pulse. The pulse compression –here quantified by the contour line at half maximum of the NR CRS spectrum in the region 200-1600 cm^{-1} (i.e. HWHM)– shows only a slight dependence on the input chirp pulse in the range between -500 fs^2 and 500 fs^2, and it decreases dramatically for larger (absolute) values of the pulse GDD. When realized in air, on the other hand, fs laser-induced filamentation has a more complex dependence on the input chirp, and the HWHM bandwidth contour shown in Fig. 3(a) remarkably presents a local minimum close to the condition of a TL pulse. Introducing a small amount of GDD in the input pulse enhances the pulse compression resulting in two local maxima of the excitation bandwidth for $\varphi_2 = 397$ fs^2 and $\varphi_2 = -492$ fs^2; the latter was found to optimize the pulse compression for ultrabroadband H_2 CRS spectroscopy in the flame. Furthermore, comparing the bandwidth of the compressed supercontinuum generated in CH_4 and in air, the higher electronic third-order susceptibility of CH_4, being almost thrice as large as that of N_2 and O_2 (see Table S1 in Supplement 1), results in a larger pulse compression via fs laser-induced filamentation. We operated the external compressor so as to optimize the pulse compression via filamentation in the flame environment, introducing a GDD of -492 fs^2 to the input pulse, which is thus stretched to ~52 fs, as measured by the NR CRS signal in Fig. 3(c), recorded in flow of a non-resonant gas (argon) at low pulse energy (i.e. without filamentation).

Figure 3(d) shows the application of the NR CRS model to estimate the duration and the residual chirp of the compressed supercontinuum generated via fs laser-induced filamentation

Optics EXPRESS

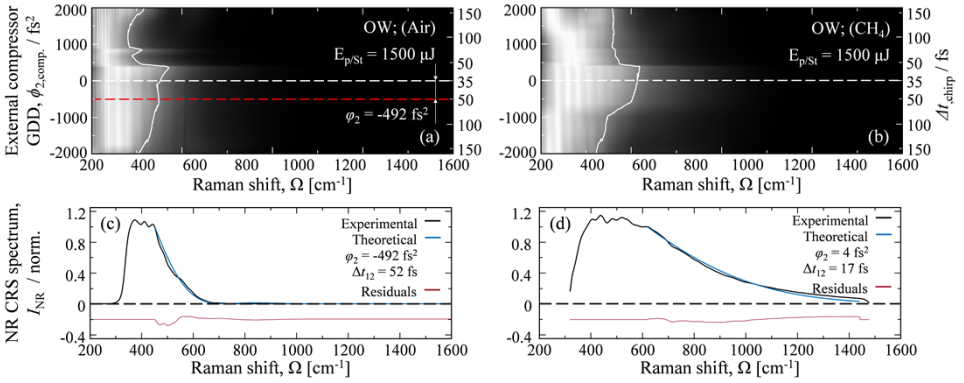

Fig. 3. Pulse compression by fs laser-induced filamentation behind the optical window. The ultrabroadband NR CRS signal is generated in room-temperature (a) air and (b) CH_4, for varying linear chirp in the input fs pump/Stokes pulse. 1000-shot-averaged spectra are shown. The white contour line identifies the HWHM excitation bandwidth. For moderate input chirp (i.e. $|\varphi_2| < 500$ fs^2) the bandwidth of the compressed supercontinuum generated in CH_4 is almost unaffected by the input chirp. In air, a local minimum in the bandwidth of the supercontinuum pulse is obtained for a TL input pulse, while two local maxima are achieved for slightly chirped pulses. The setting $\varphi_2 = -492$ fs^2 (dashed red line) of the external compressor was employed to optimize the pulse compression in the flame experiments. (c) 1000-shot-averaged NR CRS spectrum of the chirped input fs pulse optimized for pulse compression via filamentation in the flame environment (d) 1000-shot-averaged ultrabroadband NR CRS spectrum recorded in a flow of argon. The spectrum clearly displays the success of generating a compressed supercontinuum behind the optical window, which can be used for ultrabroadband CRS in enclosed spaces.

in argon (*ex-situ*): this is measured to be a near-TL pulse with a duration of 17 fs. Finally, we can estimate the impact that the optical window would have on the transmission of this supercontinuum pulse generated *ex-situ*, when employed as the pump/Stokes pulse for H_2 CRS behind the window itself. The ~424 fs^2 GDD introduced by 22 mm of BK7 glass would result in a significant stretch of the compressed supercontinuum generated *ex-situ*, to ~68 fs requiring additional phase control techniques to guarantee a sufficient excitation bandwidth and perform ultrabroadband CRS on H_2.

3.3. *In-situ referencing of the compressed supercontinuum generated in the flame*

The experimental protocol for the *in-situ* referencing [30] of the fs laser excitation of the Raman-active modes relies on the simultaneous generation of the resonant and NR CRS signals with orthogonal polarization. The theory of polarization control over the generation of the resonant and NR CRS signals is detailed in Supplement 1. We assume the polarization of our combined pump/Stokes pulse as a reference, and define the relative polarization angles of the probe, and the resonant and the NR components of the CRS signal respectively as α, β, and γ. The polarization angles of the resonant and NR CRS signals, as a function of the relative probe polarization angle, are:

$$\begin{aligned} \tan\beta &= (1-2\rho)\tan\alpha \\ \tan\gamma &= \tfrac{1}{3}\tan\alpha \end{aligned} \tag{9}$$

where ρ is the depolarization ratio of the Raman-active molecules. The functional relations in Eq. (9) are represented on the unit sphere in Fig. 1(b). Coupling Eq. (9) with the condition for simultaneous generation of cross-polarized resonant and NR CRS signals, i.e. $|\beta - \gamma| = \pi/2$, we

Optics EXPRESS

determine the required relative probe polarization angle:

$$\alpha = \tan^{-1}\left(\pm\frac{\sqrt{3}}{\sqrt{2\rho-1}}\right) \tag{10}$$

Equation (10) has real solutions only for ρ>1/2: the applicability of the *in-situ* referencing protocol is thus limited to weakly-polarized or depolarized Raman transitions. In the present work we are interested in applying the *in-situ* referencing protocol to the pure-rotational CRS spectrum of H_2, whose Raman-activity is entirely due to their anisotropic polarizability: the pure-rotational H_2 Raman spectrum is thus entirely depolarized and $\rho = 3/4$. Equation (10) then gives the relative probe polarization angle that results in cross-polarized resonant H_2 and NR CRS signals: $\alpha = \tan^{-1}\sqrt{6}$.

Figure 4(a) shows the average NR CRS spectra acquired *in-situ* at each measurement location across the flame front (see Fig. 1(d)) and is compared to the average NR CRS spectrum generated *ex-situ* in room-temperature argon (same as Fig. 3 (d)). The ultrabroadband CRS signal spans over 1600 cm^{-1}, and the band-pass filter is tuned to transmit the spectral region ~300-1500 cm^{-1}. The comparison between the fs laser excitation efficiency, as mapped by the NR signal generated *in-situ versus ex-situ*, illustrates the significant impact of the boundary conditions to the supercontinuum generation via *in-situ* filamentation in the flame. The instantaneous bandwidth of the compressed supercontinuum is here defined as half-width-at-half-maximum (HWHM) of the signal over the measured spectral range ~300-1500 cm^{-1}, and it is measured to be 394 cm^{-1} for the compressed supercontinuum generated *ex-situ* in argon. For comparison the excitation bandwidth provided by a 35 fs TL pump/Stokes pulse over the spectral range ~300-1500 cm^{-1} is 126 cm^{-1}. In the flame, the bandwidth of the supercontinuum varies from 206 cm^{-1} at y = 0 mm to 136 cm^{-1} at y = 8 mm, corresponding to a pulse duration of respectively 26 fs (GDD = 100 fs^2) and 30 fs (GDD = 100 fs^2). This reduction in the pulse compression is due to the lower effective refractive index of the optical medium along the filament propagation across the flame front. This has a comparable effect on the two non-linear optical effects underlying fs laser-induced filamentation, i.e. optical Kerr effect and multi-photon ionization. The lesser effective refractive index of the optical medium at higher temperatures determines a reduction of the self-phase modulation of the fs pulse and of the plasma density in the filament, resulting in a lesser pulse compression. This effect is of course highly dependent on the spatio-temporal boundary conditions to the filamentation process, requiring the *in-situ* referencing protocol to faithfully map the excitation efficiency of the different Raman transitions. The locality of the supercontinuum generation is moreover evident looking at the progressive reduction in the excitation bandwidth from the center of the burner to its rim, due to the three-dimensional curvature of the conical flame.

3.4. Pure-rotational H_2 CSR spectroscopy

Figure 4(b) presents the single-shot resonant H_2 CRS spectra acquired across the flame front. Six rotational lines of H_2 –from O(2) at 354 cm^{-1} to O(7) at 1447 cm^{-1}– were detected simultaneously, at high temperature, in the detection bandwidth of the spectrometer and within the dynamic range of the sCMOS detector. The rotational lines in the resonant spectra show the characteristic alternating intensity of even and odd lines, in accordance with the degeneracy of the single and triplet spin states [29]. The progression along the transverse axis clearly shows the shift in the rotational Boltzmann population of the H_2 molecules with the increasing temperature across the flame front. At y = 0 the relatively low temperature of the molecular ensemble results in the lower rotational states, in particular J = 1←3, being the most populated. Moving towards the rim of the burner, the increment in temperature results in the shift of the rotational population toward higher energy states: for y > 4.5 mm the transition J = 3←5 dominates the rotational spectrum.

Optics EXPRESS

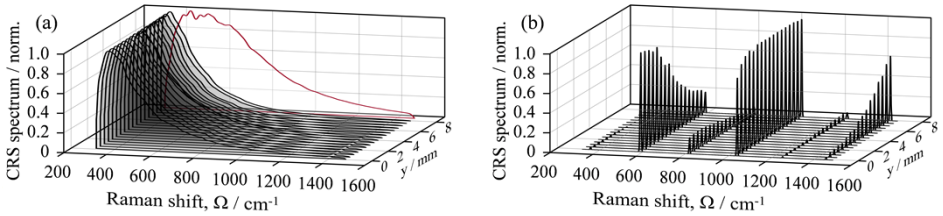

Fig. 4. (a) Ultrabroadband NR CRS spectra acquired *ex-situ* in room temperature argon (red curve) and *in-situ* at the different measurement locations across the flame front (black curves). Each curve represents the average of 1200 single-shot spectra. (b) Single-shot pure-rotational H_2 CRS spectra acquired across the flame front of a laminar H_2/air diffusion flame. Up to six rotational lines are detected simultaneously within the dynamic range of the sCMOS detector.

The single-shot H_2 spectra are fitted to a time-domain model similar to that presented in Ref. [29] (details in Supplement 1) to extract the local temperature across the flame front. An example of the spectral fit is shown in Fig. 5(a) and Fig. 5(b), where the comparison between the conventional *ex-situ* and the *in-situ* referencing protocol is presented. The larger bandwidth of the NR CRS signal generated *ex-situ* in room-temperature argon (Fig. 5(a)) overestimates the effective excitation efficiency of the higher Raman transitions, resulting in spectral cooling. This behavior severely skews the envelope of the Raman spectrum so that, even for the best-fitting temperature, the *ex-situ*-referenced spectrum does not follow Boltzmann distribution, as illustrated by the large misfit of most rotational lines. The use of the correct spectral reference, provided by the NR signal generated *in-situ* (Fig. 5(b)), is thus critical to perform quantitative spectroscopy on the pure-rotational H_2 spectrum. The temperature profile across the flame front, as measured by H_2 CRS thermometry, is shown in Fig. 5(c), along with the validation measurements performed by conventional N_2 CRS thermometry. As N_2-dilution of the H_2 flow is employed, conventional N_2 CRS measurements are possible on both sides of the flame front, allowing for a complete reconstruction of the temperature profile. H_2 on the other hand is rapidly consumed in the chemical reaction, so that the H_2 CRS signal rapidly decreases moving towards the burner rim, for the combined effect of the increasing temperature and the reduced H_2 concentration: ultrabroadband H_2 CRS measurements were performed up to $y = 8$ mm. The temperatures measured by N_2 CRS and H_2 CRS are well in agreement when the *in-situ* NR signal is employed for the spectral referencing of the ultrabroadband H_2 CRS spectra: the accuracy of the H_2 thermometry is below 1% for most measurement locations across the flame front. H_2 CRS thermometry employing *ex-situ* referencing, on the other hand, results in a significant bias (up to 80%) towards lower temperatures at all the measurement locations, as shown in Fig. 5(d).

The precision of ultrabroadband H_2 CRS thermometry was estimated as the standard deviation of the measured temperature over a sample of 1200 single-shot spectra. This is comparable to that of conventional N_2 CRS, varying in the range ~1-3%, for $y \leq 6.5$ mm, while it is negatively impacted by the H_2 consumption in the reaction zone of the flame, with a significant reduction of the signal intensity. At the last three measurement locations, this abatement of the signal impaired the detection of the O(2) line (see Fig. 4(b)), and the signal-to-background ratio (SBR) of the O(6) line was reduced to ~2. At the last measurement point, the O(5) line was barely detectable (SBR~1.3) and the spectral fit only relied on four lines, reducing the precision to ~9%. These temperature measurements are in good agreement with the values reported by Toro *et al* for a similar laminar H_2/air diffusion flame [45].

Ultrabroadband CRS further provides new insights in the molecular transport processes taking place in the measurement environment presented here. Figure 6(a) shows the experimental temperature and relative H_2/N_2 concentration profiles, measured by ultrabroadband CRS across

Optics EXPRESS

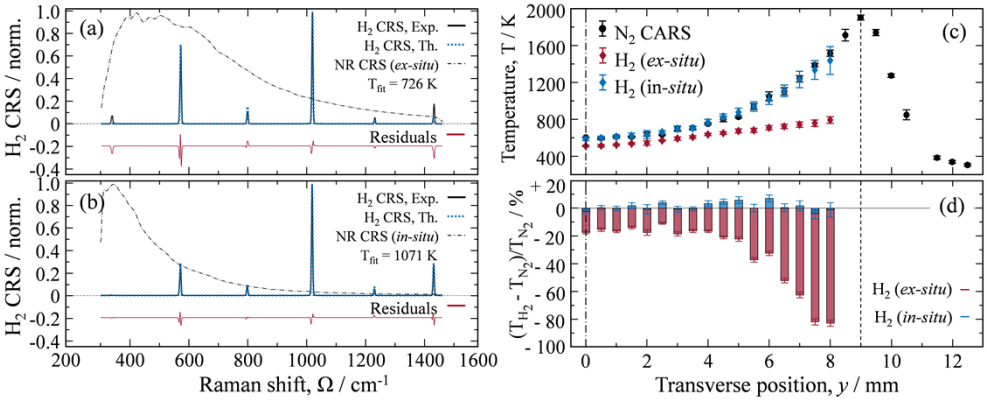

Fig. 5. (a) Single-shot experimental H_2 CRS spectrum (solid line) acquired in the flame at y = 6 mm, referenced by the NR CRS (dot-dashed line) spectrum acquired *ex-situ* in argon, and comparison to the time-domain H_2 CRS model (dotted line) to fit the Boltzmann distribution. (b) The same experimental spectrum is referenced by the NR CRS spectrum simultaneously acquired *in-situ*, and fitted to the time-domain H_2 CRS model. (c) Temperature profile measured by conventional pure-rotational N_2 CRS and ultrabroadband H_2 CRS spectroscopy. (d) Comparison of the measurement accuracy of H_2 CRS thermometry for the *ex-situ* and *in-situ* referencing protocols: the standard (*ex-situ*) protocol results in a consistent underestimation of the H_2 temperature.

the flame front: moving from the center of the burner to the chemical reaction zone, the H_2 concentration significantly reduces, from 50% to 40%, while the temperature presents only a minor increment up to y = 3.5 mm as shown in Fig. 6(b). This small change in temperature (~57 K) is attributed to heat transfer from the high-temperature reaction zone, rather than to the onset of the chemical reaction itself: H_2 is not consumed in this region, but it is rapidly transported towards the reaction zone, owing to its large mass diffusivity [31]. To the best of our knowledge, this represents the first direct observation of molecular preferential diffusion in a H_2/air flame.

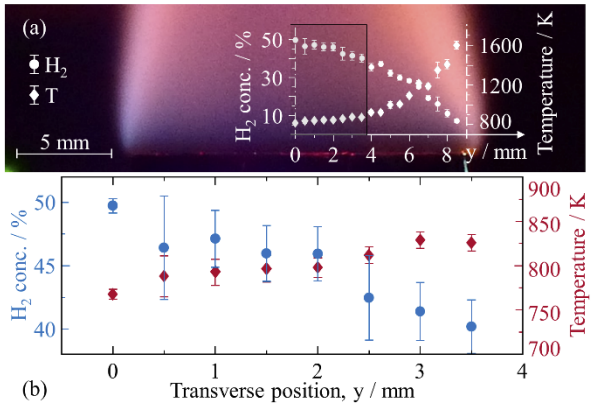

Fig. 6. (a) Simultaneous CRS measurement of the temperature and relative H_2/N_2 concentration across the flame front (1 mm above the nozzle). The black box represents the area of interest for H_2 preferential diffusion. (a) A significant reduction of the H_2 concentration, from 50% at y = 0 mm to 40% at y = 3.5 mm, is measured in the face of an almost constant temperature profile and is thus attributed to preferential diffusion.

Optics EXPRESS

4. Conclusions

A novel approach to ultrabroadband CRS is proposed as a straightforward pathway to rotational H_2 spectroscopy in closed environments, such as high-pressure combustors or chemical reactors. The investigation of H_2 chemistry by time-resolved coherent Raman techniques requires a compressed supercontinuum to generate coherence between the widely spaced states in the rotational energy manifold [29], but is hindered by the introduction of non-linear contributions to its spectral phase. To date ultrabroadband fs/ps H_2 CRS has not been applied in closed measurement scenarios.

The technique here proposed is based on the *in-situ* generation, use and referencing of the coherent excitation provided by supercontinuum compression in fs laser-induced filamentation. The 35 fs output of a regenerative fs laser amplifier was negatively chirped before its transmission through a 22 mm BK7 glass window, resulting in a residual negative chirp of ~490 fs^2: this value is experimentally demonstrated to optimize the multiphoton ionization and the optical Kerr effects that underpin the pulse compression in the filamentation process. We have shown that the NR CRS signal, which has often been considered detrimental to CRS, with much effort dedicated to its suppression [24,46], not only maps the efficiency of the coherent excitation delivered by the pump/Stokes pulse, but can be effectively used to perform spectral autocorrelation measurements of the pump/Stokes pulse and to characterize its transmission through optical media. This result is particularly powerful when combined to the last piece of the present diagnostic puzzle: the *in-situ* referencing protocol to monitor the ultrabroadband spectral excitation delivered by the compressed supercontinuum. This novel experimental protocol utilizes polarization control over the input laser fields to generate the resonant and NR signals with relative orthogonal polarization, and realizes their simultaneous separated detection in a polarization-sensitive coherent imaging spectrometer. Altogether *in-situ* generation, *in-situ* use, and *in-situ* referencing of the ultrabroadband coherent Raman excitation define a new diagnostics to investigate the rotational energy distribution in gaseous H_2.

Ultrabroadband H_2 CRS measurements were demonstrated over a wide range of temperature and H_2 concentration across a canonical H_2/air diffusion flame (Fig. 5), and validated against conventional N_2 CRS thermometry. The potential of our technique is further exemplified by what, to the best of our knowledge, is the first direct observation of H_2 preferential diffusion in H_2/air flames. The effect of the mass transport mechanism for the lightweight H_2 molecules is uncovered by the spatial mismatch of the temperature and relative H_2/N_2 concentration, as measured by pure-rotational CRS (Fig. 6). Although this configuration is designed for rather large-scale combustor test rigs (approximately 0.5 m in width), it can be extended to smaller-scale housings as in Ref. [26], provided that the numerical aperture and therefore the filament properties are maintained. For instance, the input beam diameter can be modified accordingly to reduce the field irradiance inside the window when short focal-length optics are required. We prospect the far ranging application of this diagnostics in all the research fields where H_2 chemistry plays a key role, from novel sustainable combustion technologies to methane reforming for H_2 production. To name one, liquid oxygen/gaseous H_2 rocket combustion is a thriving research field with application to low-Earth commercialization and sustainable space exploration [47]. Our technique has clear advantages in such high-pressure environments, where both the fs pulse compression and the coherent Raman excitations are enhanced, while time-resolved measurements can be realized probing the Raman coherences below the collisional time-scale.

Funding. Nederlandse Organisatie voor Wetenschappelijk Onderzoek (15690).

Acknowledgements. We gratefully acknowledge the financial support provided by the Netherlands Organization for Scientific Research (NWO), obtained through a Vidi grant in the Applied and Engineering Sciences domain (AES) (15690). A. Bohlin is thankful for support through the RIT (Space for Innovation and Growth) project/European Regional Development Fond in Kiruna, Sweden.

Disclosures. The authors declare no conflicts of interest.

Optics EXPRESS

Data availability. Data underlying the results presented in this paper are not publicly available at this time, but may be obtained from the authors upon reasonable request.

Supplemental document. See Supplement 1 for supporting content.

References

1. "Hydrogen on the rise," Nat. Energy 1, 16127 (2016).
2. Y. Shagam, A. Klein, W. Skomorowski, R. Yun, V. Averbukh, C. P. Koch, and E. Narevicius, "Molecular hydrogen interacts more strongly when rotationally excited at low temperatures leading to faster reactions," Nat. Chem. **7**(11), 921–926 (2015).
3. S. A. Lahankar, J. Zhang, K. G. McKendrick, and T. K. Minton, "Product-state-resolved dynamics of the elementary reaction of atomic oxygen with molecular hydrogen, $O(^3P) + D2 \rightarrow OD(X\,^2\Pi) + D$," Nat. Chem. **5**(4), 315–319 (2013).
4. N. G. Kling, S. Díaz-Tendero, R. Obaid, M. R. Disla, H. Xiong, M. Sundberg, S. D. Khosravi, M. Davino, P. Drach, A. M. Carroll, T. Osipov, F. Martín, and N. Berrah, "Time-resolved molecular dynamics of single and double hydrogen migration in ethanol," Nat. Commun. **10**(1), 2813 (2019).
5. R. P. Lucht, "Femtosecond lasers for molecular measurements," Science **316**(5822), 207–208 (2007).
6. D. A. Greenhalgh, "Raman: An eye for combustion studies," Nature **291**(5816), 535–536 (1981).
7. S. Roy, J. R. Gord, and A. K. Patnaik, "Recent advances in coherent anti-Stokes Raman scattering spectroscopy: Fundamental developments and applications in reacting flows," Prog. Energy Combust. Sci. **36**(2), 280–306 (2010).
8. C. E. Dedic, T. R. Meyer, and J. B. Michael, "Single-shot ultrafast coherent anti-Stokes Raman scattering of vibrational/rotational nonequilibrium," Optica **4**(5), 563–570 (2017).
9. T. Chen, B. Goldberg, B. Patterson, E. Kolemen, C. Kliewer, K. Olemen, J. Yiguang, and C. H. J. K. Liewer, "1-D imaging of rotation-vibration non-equilibrium from pure rotational ultrafast coherent anti-Stokes Raman scattering," Opt. Lett. **45**(15), 4252–4255 (2020).
10. I. R. Beattie, T. R. Gilson, and D. A. Greenhalgh, "Low frequency coherent anti-Stokes Raman spectroscopy of air," Nature **276**(5686), 378–379 (1978).
11. R. L. Farrow and L. A. Rahn, "Optical Stark Splitting of Rotational Raman Transitions," Phys. Rev. Lett. **48**(6), 395–398 (1982).
12. F. Benabid, F. Couny, J. C. Knight, T. A. Birks, and P. S. J. Russell, "Compact, stable and efficient all-fibre gas cells using hollow-core photonic crystal fibres," Nature **434**(7032), 488–491 (2005).
13. R. L. Farrow and L. a Rahn, "Measurement of the self-broadening of the H_2 Q(0-5) Raman transitions from 295 to 1000 K," Phys. Rev. A **43**(11), 6075–6088 (1991).
14. V. Bergmann and W. Stricker, "H_2 CARS thermometry in a fuel-rich, premixed, laminar CH_4/air flame in the pressure range between 5 and 40 bar," Appl. Phys. B **61**(1), 49–57 (1995).
15. V. A. Shakhatov, O. De Pascale, M. Capitelli, K. Hassouni, G. Lombardi, and A. Gicquel, "Measurement of vibrational, gas, and rotational temperatures of H_2 ($X\,^1\Sigma_g^+$) in radio frequency inductive discharge plasma by multiplex coherent anti-Stokes Raman scattering spectroscopy technique," Phys. Plasmas **12**(2), 023504 (2005).
16. A. H. Zewail, "Laser Femtochemistry," Science **242**(4886), 1645–1653 (1988).
17. T. Lang, K. Kompa, and M. Motzkus, "Femtosecond CARS on H_2," Chem. Phys. Lett. **310**(1-2), 65–72 (1999).
18. H. Tran, P. Joubert, L. Bonamy, B. Lavorel, V. Renard, F. Chaussard, O. Faucher, and B. Sinardet, "Femtosecond time resolved coherent anti-Stokes Raman spectroscopy: Experiment and modelization of speed memory effects on H_2-N_2 mixtures in the collision regime," J. Chem. Phys. **122**(19), 194317 (2005).
19. S. A. Magnitskiĭ and V. G. Tunkin, "Determination of the Dicke Narrowing in Gaseous Hydrogen By Direct Measurement of the Dephasing Time," Sov. J. quantum Electron. **11**(9), 1218–1220 (1981).
20. W. D. Kulatilaka, P. S. Hsu, H. U. Stauffer, J. R. Gord, and S. Roy, "Direct measurement of rotationally resolved H_2 Q-branch Raman coherence lifetimes using time-resolved picosecond coherent anti-Stokes Raman scattering," Appl. Phys. Lett. **97**(8), 081112 (2010).
21. M. O. Scully, G. W. Kattawar, R. P. Lucht, T. Opatrný, H. Pilloff, A. Rebane, A. V. Sokolov, and M. S. Zubairy, "FAST CARS: Engineering a laser spectroscopic technique for rapid identification of bacterial spores," Proc. Natl. Acad. Sci. U. S. A. **99**(17), 10994–11001 (2002).
22. D. Pestov, R. K. Murawski, G. O. Ariunbold, X. Wang, M. Zhi, A. V. Sokolov, V. A. Sautenkov, Y. V. Rostovtsev, A. Dogariu, Y. Huang, and M. O. Scully, "Optimizing the laser-pulse configuration for coherent Raman spectroscopy," Science **316**(5822), 265–268 (2007).
23. B. D. Prince, A. Chakraborty, B. M. Prince, and H. U. Stauffer, "Development of simultaneous frequency- and time-resolved coherent anti-Stokes Raman scattering for ultrafast detection of molecular Raman spectra," J. Chem. Phys. **125**(4), 044502 (2006).
24. N. Dudovich, D. Oron, and Y. Silberberg, "Single-pulse coherently controlled nonlinear Raman spectroscopy and microscopy," Nature **418**(6897), 512–514 (2002).
25. A. Bohlin and C. J. Kliewer, "Single-shot hyperspectral coherent Raman planar imaging in the range 0-4200 cm^{-1}," Appl. Phys. Lett. **105**(16), 161111 (2014).
26. D. R. Richardson, S. P. Kearney, and D. R. Guildenbecher, "Post-detonation fireball thermometry via femtosecond-picosecond coherent anti-Stokes Raman Scattering (CARS)," Proc. Combust. Inst. **38**(1), 1657–1664 (2021).

Optics EXPRESS

27. J. H. Odhner, D. A. Romanov, and R. J. Levis, "Rovibrational Wave-Packet Dispersion during Femtosecond Laser Filamentation in Air," Phys. Rev. Lett. **103**(7), 075005 (2009).
28. A. Bohlin, B. D. Patterson, and C. J. Kliewer, "Communication: Simplified two-beam rotational CARS signal generation demonstrated in 1D," J. Chem. Phys. **138**(8), 081102 (2013).
29. T. L. Courtney, A. Bohlin, B. D. Patterson, and C. J. Kliewer, "Pure-rotational H_2 thermometry by ultrabroadband coherent anti-stokes Raman spectroscopy," J. Chem. Phys. **146**(22), 224202 (2017).
30. F. Mazza, L. Castellanos, D. Kliukin, and A. Bohlin, "Coherent Raman imaging thermometry with in-situ referencing of the impulsive excitation efficiency," Proc. Combust. Inst. **38**(1), 1895–1904 (2021).
31. R. S. Barlow, M. J. Dunn, M. S. Sweeney, and S. Hochgreb, "Effects of preferential transport in turbulent bluff-body-stabilized lean premixed CH_4/air flames," Combust. Flame **159**(8), 2563–2575 (2012).
32. D. Meshulach and Y. Silberberg, "Coherent quantum control of two-photon transitions by a femtosecond laser pulse," Nature **396**(6708), 239–242 (1998).
33. A. A. Lanin, I. V. Fedotov, A. B. Fedotov, D. A. Sidorov-Biryukov, and A. M. Zheltikov, "The phase-controlled Raman effect," Sci. Rep. **3**(1), 1842 (2013).
34. U. Gaubatz, P. Rudecki, S. Schiemann, and K. Bergmann, "Population transfer between molecular vibrational levels by stimulated Raman scattering with partially overlapping laserfields. A new concept and experimental results," J. Chem. Phys. **92**(9), 5363–5376 (1990).
35. S. Zhdanovich, E. A. Shapiro, M. Shapiro, J. W. Hepburn, and V. Milner, "Population transfer between two quantum states by piecewise chirping of femtosecond pulses: Theory and experiment," Phys. Rev. Lett. **100**(10), 103004 (2008).
36. C. H. Camp, Y. J. Lee, J. M. Heddleston, C. M. Hartshorn, A. R. H. Walker, J. N. Rich, J. D. Lathia, and M. T. Cicerone, "High-speed coherent Raman fingerprint imaging of biological tissues," Nat. Photonics **8**(8), 627–634 (2014).
37. F. Mazza, N. Griffioen, L. Castellanos, D. Kliukin, and A. Bohlin, "High-temperature rotational-vibrational O_2-CO_2 coherent Raman spectroscopy with ultrabroadband femtosecond laser excitation generated in-situ," Combust. Flame **237**, 111738 (2022).
38. S. Rostami, J.-C. Diels, and L. Arissian, "Polarization evolution of ultrashort pulses in air," Opt. Express **23**(3), 3299–3307 (2015).
39. A. H. Sheinfux, E. Schleifer, J. Papeer, G. Fibich, B. Ilan, and A. Zigler, "Measuring the stability of polarization orientation in high intensity laser filaments in air," Appl. Phys. Lett. **101**(20), 201105 (2012).
40. E. T. J. Nibbering, D. A. Wiersma, and K. Duppen, "Ultrafast Nonlinear Spectroscopy with Chirped Optical Pulses," Phys. Rev. Lett. **68**(4), 514–517 (1992).
41. Y. J. Yan and S. Mukamel, "Pulse shaping and coherent Raman spectroscopy in condensed phases," J. Chem. Phys. **94**(2), 997–1005 (1991).
42. T. Hellerer, A. M. K. Enejder, and A. Zumbusch, "Spectral focusing: High spectral resolution spectroscopy with broad-bandwidth laser pulses," Appl. Phys. Lett. **85**(1), 25–27 (2004).
43. F. Théberge, N. Aközbek, W. Liu, A. Becker, and S. L. Chin, "Tunable ultrashort laser pulses generated through filamentation in gases," Phys. Rev. Lett. **97**(2), 023904 (2006).
44. A. Mysyrowicz, A. Couairon, and U. Keller, "Self-compression of optical laser pulses by filamentation," New J. Phys. **10**(2), 025023 (2008).
45. V. V Toro, A. V Mokhov, H. B. Levinsky, and M. D. Smooke, "Combined experimental and computational study of laminar, axisymmetric hydrogen–air diffusion flames," Proc. Combust. Inst. **30**(1), 485–492 (2005).
46. L. Gong, W. Zheng, Y. Ma, and Z. Huang, "Higher-order coherent anti-Stokes Raman scattering microscopy realizes label-free super-resolution vibrational imaging," Nat. Photonics **14**(2), 115–122 (2020).
47. F. Grisch, P. Bouchardy, and W. Clauss, "CARS thermometry in high pressure rocket combustors," Aerosp. Sci. Technol. **7**(4), 317–330 (2003).